TRENDS IN SCIENCES 2026; 23(12): 14120
https://doi.org/10.48048/tis.2026.14120 RESEARCH ARTICLE

In-situ Transformation of MoS_2 and Waste Eggshells into $CaMoO_4$-based Composite: Synergistic Mechanisms for Organic and Inorganic Pollutant Remediation

Chonlada Dechakiatkrai Theerakarunwong[1,*], Waraporn Chuaychai[2], Rutairat Photi[3] and Chaikarn Leawhiran[4]

[1]*Chemistry Program, Department of Science, Faculty of Science and Technology, Nakhon Sawan Rajabhat University, Nakhon Sawan 60000, Thailand*
[2]*Biology Program, Department of Science, Faculty of Science and Technology, Nakhon Sawan Rajabhat University, Nakhon Sawan 60000, Thailand*
[3]*Environmental Science Program, Department of Science, Faculty of Science and Technology, Nakhon Sawan Rajabhat University, Nakhon Sawan 60000, Thailand*
[4]*Department of Physics and Materials Science, Faculty of Science, Chiang Mai University, Chiang Mai 50200, Thailand*

([*]Corresponding author's e-mail: chonlada.d@nsru.ac.th)

Received: 17 April 2026, Revised: 9 June 2026, Accepted: 19 June 2026, Published: 5 August 2026

Abstract

In this work, a $CaMoO_4$-based composite was synthesized via the in-situ transformation of MoS_2 and eggshell-derived $CaCO_3$ precursors. $CaMoO_4$-based composite-based composite was formed in-situ during microwave-assisted hydrothermal treatment through direct phase transformation of the precursor mixture. The phase transformation was confirmed by XRD analysis, showing the conversion into a crystalline scheelite $CaMoO_4$-based composite structure, while SEM and TEM observations revealed a porous, cauliflower-like morphology composed of integrated nanosheets. The in-situ transformation was further validated by FT-IR and BET analyses, which showed a significant enhancement in the specific surface area to 85.5 m^2 g^{-1} for the 7 wt% $CaCO_3$-loaded sample. This synergistic adsorption-photocatalytic/photoreduction process of $CaMoO_4$-based composite proved effective in removing methylene blue (MB), methyl orange (MO), lead (II) ion, and chromium (VI) ion, demonstrating superior removal rates and stability over 3 cycles. Kinetic studies followed the pseudo-first-order model, with the highest rate constant for MB at 0.0480 min^{-1}. Scavenging experiments identified $\cdot O_2^-$ as the primary reactive species driving the degradation process. Furthermore, a 44.65% TOC removal confirmed significant mineralization, demonstrating the catalyst's dual-functionality in effectively remediating both organic and inorganic pollutants. Phytotoxicity evaluation using *H. verticillata* revealed that the Ca^{2+} ions released from the catalyst effectively mitigated heavy metal stress by reducing the uptake of Pb(II) and Cr(VI), confirming the environmental safety of the treated water. This hybrid composite exhibits significant potential for environmental applications, particularly for the efficient utilization of visible or solar energy in wastewater remediation.

Keywords: Photocatalysis, Photoreduction, Adsorption, $CaCO_3$, MoS_2, $CaMoO_4$, Heavy metal, Dye, Textile

Introduction

Water pollution caused by organic synthetic dyes and heavy metal ions represents a serious environmental and health hazard. These contaminants are highly persistent, accumulate through the food chain, and can cause severe toxicity to living organisms [1,2]. To treat complex industrial wastewater, various remediation technologies have been developed, including physical, chemical, and biological processes. While physical

adsorption is simple and low-cost, it only transfers pollutants to a solid matrix without destroying their structures [3,4]. Biological treatment is highly eco-friendly and cost-effective for large-scale operations, but it suffers from slow degradation kinetics and is highly sensitive to the acute toxicity of heavy metals and concentrated chemical dyes [5,6]. In contrast, advanced oxidation processes (AOPs) represent a promising chemical approach that utilizes highly reactive radicals to break down toxic molecules into harmless end products. As a subclass of AOPs, heterogeneous photocatalysis uses solar energy to drive both organic dye degradation and heavy metal reduction simultaneously [7,8].

Molybdenum disulfide (MoS_2) based nanomaterials are becoming increasingly recognized due to their potential as efficient photocatalysts, particularly in the presence of near-infrared (NIR) light. The oxygen defect structure of the MoS_2 semiconductor provides significant photo-absorption over a broad wavelength range spanning the ultraviolet (UV), visible (Vis), and near-infrared regions, which is equivalent to around half of the electromagnetic radiation emitted by the sun [9-13]. The conduction and valence bands of MoS_2 are larger than the oxidation and reduction potentials of the H_2/H_2O reaction, allowing MoS_2 to photocatalyze the removal of organic contaminants [12-14].

Currently, a significant amount of research is focused on utilizing biowaste in combination with photocatalyst nanomaterials for environmental benefits as a result of sustainability research [15]. Eggshell waste is a common byproduct of food processing, frequently disposed of after usage. The eggshell and its membrane have various applications in different fields, such as electrochemistry, catalysis, adsorption, food supplements, and medical uses [16-19]. Thus, many researchers are now focused on the use of eggshells in a variety of environmentally friendly processes. The porous structure of eggshell makes it a desirable substance to serve as an adsorbent material [20]. According to the literature reviews, modified eggshell as a beneficial adsorbent could potentially be used to treat water that contains organic dyes and inorganic heavy metals [21,22]. Furthermore, they can serve as a cost-effective source of calcium ions for creating composites that are utilized in photocatalysis. Eggshell residues have been used in photocatalytic applications as a support for semiconductor materials or as a template for synthesizing semiconductor samples. When exposed to light, these materials generate holes and electrons that can trigger oxidative and reductive reactions. On the other hand, a recombination process can occur and reduce the photocatalytic efficiency [19,23,24].

To address the charge recombination issue of pure semiconductors, calcium-based composites have recently gained attention. The interaction between calcium species and molybdate can lead to the formation of $CaMoO_4$, a scheelite-structured material known for its enhanced light absorption and photocatalytic stability [25]. While eggshell-derived $CaCO_3$ is often used as a template or adsorbent, its role as a reactive precursor for in-situ transformation into $CaMoO_4$ presents a pathway for developing efficient catalysts. Furthermore, the residual $CaCO_3$ structure may serve as an interfacial support, helping to stabilize the surface potentials during multi-component interactions [26,27]. The in-situ formation of a $MoS_2/CaMoO_4$ heterojunction enhances light absorption and facilitates charge separation, thereby suppressing electron-hole recombination and promoting the generation of reactive species involved in pollutant degradation [19,28]. While previous studies have utilized eggshell waste as a sustainable calcium precursor for the synthesis of $CaMoO_4$, these conventional methods typically involve multi-step chemical extraction and ex-situ precipitation processes, which may promote particle agglomeration and reduce control over the resulting microstructure [29].

To address these processing challenges and promote sustainability, the present work utilizes a direct, one-pot hydrothermal method to react eggshell waste directly with MoS_2. Microwave-assisted hydrothermal synthesis has attracted considerable attention due to its time efficiency, energy-saving capability, promotion of direct phase conversion, and reduction of multi-step synthesis processes. This approach facilitates an in-situ transformation to form $CaMoO_4$ in the presence of MoS_2. To compare this work with previous studies using biowaste, Zhang *et al.* [30] previously developed a photocatalytic system using $PbS/CaCO_3$ composites, where the $CaCO_3$ was derived from eggshell waste for the solar light-induced degradation of tetracycline hydrochloride. Their study shed important light on the mechanisms of photocatalytic reactions involving

carbonate-based composite materials [19,28]. However, while such composites can exhibit high removal efficiency, the ecological safety of treated effluents remains an important area of evaluation. Specifically, the potential release of Mo species or other leached ions into natural aquatic environments raises valid questions regarding biocompatibility and downstream phytotoxic effects.

This study uses *Hydrilla verticillata* (*H. verticillata*) as a sensitive bioindicator and primary producer to evaluate metal bioaccumulation and physiological responses. Biological testing was also performed to assess the potential environmental effects of treated wastewater, as industrial textile effluents may contain a complex mixture of dye compounds and heavy metal co-contaminants [31,32].

The objective of this work is to investigate the in-situ transformation of MoS_2 and eggshell-derived $CaCO_3$ into $CaMoO_4$ for the simultaneous removal of synthetic dyes and heavy metal-contaminated wastewater via a synergistic adsorption-photocatalytic/photoreduction mechanism. The parameters influencing the remediation efficiency were evaluated, alongside a preliminary phytotoxicity study to confirm the environmental compatibility of the synthesized material for practical wastewater treatment.

Materials and methods

Synthesis of photocatalysts

Ammonium heptamolybdate $(NH_4)_6Mo_7O_{24}{\cdot}4H_2O$ (Sigma-Aldrich) and thiourea $SC(NH_2)_2$ (Sigma-Aldrich) were employed as precursors for MoS_2 synthesis in the ratio of 1:30 mmol, while distilled water was used as a solvent. The mixture was mixed and stirred using a magnetic stirrer for 30 min and then transferred to a Teflon-lined stainless steel autoclave reactor, which was placed in a microwave system. The reaction was carried out at 200 °C with a power of 1,800 W for 10 min. The obtained product was collected by centrifugation, washed with ethanol, dried at 70 °C for 3 h, and thoroughly ground before use.

Eggshells (ES) were collected from household waste and washed before being boiled at 100 °C for 1 h to remove organic compounds, followed by drying at 100 °C. For size reduction, ES was ground using a blender and sieved through a 100-mesh sieve. The as-prepared sample was subsequently dispersed in distilled water under ultrasonication for 30 min. The suspension was filtered to remove larger particles and dried at 70 - 80 °C for 1 h. The ES particles were subsequently calcined at 800 °C for 4 h to obtain $CaCO_3$ particles.

$CaMoO_4$ was synthesized via the microwave-assisted hydrothermal method. Typically, $CaCO_3$ and MoS_2 were separately dispersed in distilled water, where the amount of $CaCO_3$ was varied to achieve specific weight ratios (0.3, 0.5, 5, 7, 10 and 13 wt%) relative to the MoS_2 precursor. The $CaCO_3$ suspension was then added dropwise into the MoS_2 suspension under constant stirring for 1 h. The resulting mixture was transferred to a Teflon-lined stainless steel autoclave reactor and heated at 180 °C for 10 min, followed by further heating at 200 °C for 10 min under a microwave power of 1,800 W. The final product was cooled to room temperature, centrifuged, washed several times with deionized water, and dried at 70 °C for 3 h.

Characterization

High-resolution transmission electron microscopy (HR-TEM) (JEM-2100, JEOL, Tokyo, Japan) and scanning electron microscopy (SEM) (JSM-IT800) coupled with energy dispersive X-ray spectroscopy (EDX) were used to investigate the morphology and particle size of the $CaMoO_4$ powders. X-ray diffraction (XRD: Smart Lab, Rikaku) with CuKα radiation (2 kV), recorded at a scanning rate of 2°/min was used to study the phase structure and crystallinity of the powder samples. The specific surface area (SSA) was determined through nitrogen adsorption-desorption at 77 K (Quantachrome: NOVA2200E), applying Brunauer-Emmett-Teller (BET) and Barrett-Joyner-Halenda (BJH). Attenuated total reflectance - Fourier transform infrared spectroscopy (ATR-FTIR) (PerkinElmer, Waltham, MA, USA) was used to determine the functional group of the sample.

Adsorption and photocatalytic/photoreduction activities

The synthesized $CaMoO_4$-based composite photocatalysts were dispersed in an aqueous solution of mixed organic dyes (methylene blue: MB, 5 mg L^{-1}, and methyl orange: MO, 5 mg L^{-1}) and mixed metal ions (lead: Pb(II), 1 mg L^{-1}, and chromium: Cr(VI), 1 mg L^{-1}). To achieve adsorption-desorption equilibrium, the suspension was agitated for 30 min in the dark before

being exposed to 50 mW cm^{-2} at 300 watts with a light intensity wavelength between 400 and 1,100 nm. The 3 mL resultant solution was collected every 30 min and subsequently centrifuged (1,200 rpm, 5 min) and filtered before the remaining concentration of a specific contaminant was determined by using a UV-VIS spectrophotometer (UV-1280, Shimazu, Kyoto, Japan). The loading amount of $CaCO_3$, contact time, pH, initial concentration, and type of light source (synthetic and natural light) were all explored as factors affecting removal efficiency. The light intensity was measured by a digital LUX light meter (TES-1339R, China). Furthermore, recycling, TOC, scavenging and kinetic study were also carried out. The experiments were performed in triplicate to evaluate reproducibility. Where applicable, data are presented as mean ± standard deviation (SD), with SD values ranging from 0.31 to 2.60, indicating good agreement among replicates.

Toxicity assessment of treated textile wastewater for plants

To investigate the toxicity of treated wastewater to plants, *H. verticillate* was planted in treated effluent for 30 days, with treated wastewater added when necessary. Treated wastewater from 2 sampling sites was compared to a control group consisting of synthetic dyes containing an adequate amount of metal. In each container, 3 replicates of the plant were planted. Plants were collected, washed, and dried at the end of the treatment period before metal contamination of the plants was evaluated. To investigate the metal content of plant samples, 2 g of dried samples were weighed individually and placed in a Teflon-lined stainless steel autoclave reactor. The sample was digested using a microwave-assisted hydrothermal technique with 20 mL of 25% (v/v) HNO_3. After cooling to room temperature, the extracted sample was filtered through Whatman No.1 filter paper and diluted to 25 mL with 1% v/v HNO_3. Residual Pb(II), Cr(VI), Ca and Mo concentrations in plant tissues were determined using atomic absorption spectrometry (AAS, PinAAcle 900T, PerkinElmer, USA).

Results and discussion

Morphology and structure characterization

Figure 1 depicts the XRD pattern of MoS_2, $CaCO_3$, and $CaMoO_4$-based composite. The diffraction pattern of MoS_2 exhibited broad low-intensity peak, indicating low crystallinity or nanoscale crystal size of the synthesized MoS_2, while suggesting the presence of stacking disorder. Typically, MoS_2 exhibits characteristic peaks at 2θ = 14.5°, 29.02°, 34.88°, and 39.55°, corresponding to the (002), (100), (102), and (103) planes of the pure hexagonal MoS_2 phase (JCPDS card no. 03-065-0160). However, the peak at ~14° is significantly broadened, which is consistent with TEM observations of restacked aggregates in the form of disordered clumps rather than well-defined single-crystal plates. Additionally, diffraction peaks observed in the ranges of 15° - 18° and 25° - 28° are attributed to intermediate MoO_x phases, indicating incomplete conversion to MoS_2. This suggests partial formation of MoS_2 with residual oxide phases, likely due to insufficient sulfurization caused by a microwave heating time of 10 min.

$CaCO_3$ exhibited sharp diffraction peaks indexed to rhombohedral $CaCO_3$ (JCPDS No. 01-072-1652, space group = R − 3c, a = b = 0.499 nm, c = 0.17002 nm, and $\alpha = \beta = 90°$, $\gamma = 120°$), confirming its high crystallinity. Notably, the 0.3-10 wt% $CaMoO_4$-based composite composites showed a set of intense reflections in good agreement with tetragonal $CaMoO_4$-based composite (JCPDS No. 01-085-0585, space group = I41/a, a = b = 0.52260 nm, c = 0.1143 nm and $\alpha = \beta = \gamma = 90°$), with prominent peaks indexed to the (101), (112), (004), (200), (204), and (220) planes. The dominance of $CaMoO_4$-based composite peaks indicates that the microwave-hydrothermal treatment promotes an in-situ phase transformation rather than simple physical mixing. Furthermore, increasing $CaCO_3$ loading was found to enhance both the intensity and crystallinity of the $CaMoO_4$-based composite phase.

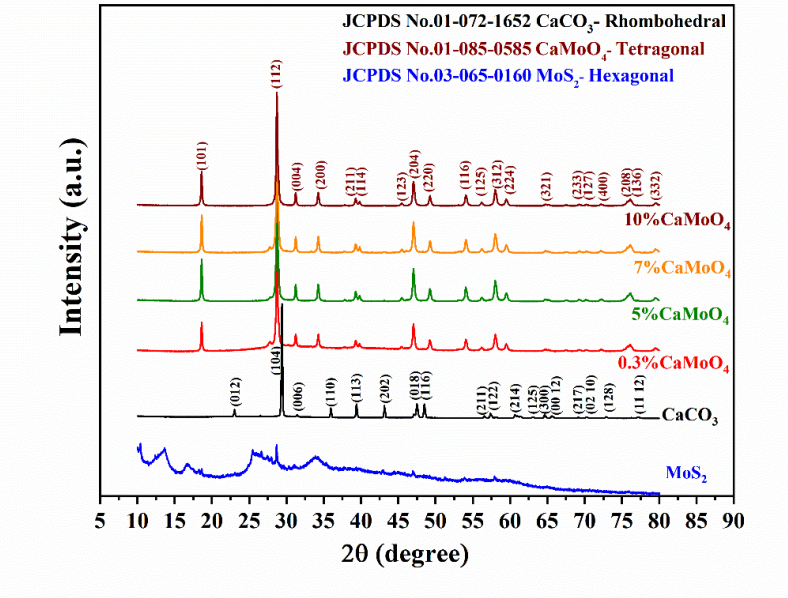


Figure 1 XRD patterns of pure MoS_2, eggshell-derived $CaCO_3$, and 0.3 - 10 wt% $CaMoO_4$-based composite. The diffraction peaks indicate the coexistence of the hexagonal MoS_2 phase and the crystalline calcite structure of $CaCO_3$. The in-situ transformation and growth of the tetragonal scheelite $CaMoO_4$ phase is confirmed by the appearance of its characteristic reflections, which exhibit a controlled increase in diffraction peak intensities as a function of the calcium precursor loading.

From the results, **Figure 2** shows the BF-TEM and HR-TEM microstructures, including the SAED patterns of $CaCO_3$, MoS_2, and 7 wt% $CaMoO_4$-based composites. The $CaCO_3$ exhibits aggregated nanoscale domains with HR-TEM lattice fringes with multiple d-spacings (~0.246 nm for (110), ~0.304 - 0.300 nm for (104), ~0.210 nm for (113), and ~0.180 nm for (110)), indicating multiple crystallographic orientations within the agglomerates, consistent with the SAED pattern exhibiting polycrystalline ring/spot features indexed to multiple $CaCO_3$ planes (**Figures 2(a) - 2(b)**). For MoS_2, extensive agglomerated clusters containing numerous tiny layered domains that have undergone restacking are observed (**Figures 2(c) - 2(d)**). This observation agrees with the XRD results, which displayed broad diffraction patterns rather than sharp peaks, which is consistent with nanosized crystallites. The SAED pattern shows a diffuse spot or halo appearance, implying low crystallinity, which may be associated with increased edge or defect-related surface sites. However, HR-TEM indicates non-uniform domains and partial restacking. For the 7 wt% $CaMoO_4$-based composite, the BF-TEM image (**Figure 2(e)**) shows a hierarchical structure in which the wrinkled nanosheet-like morphology of the MoS_2 precursor is partially retained. In addition, nanosized $CaMoO_4$-based composite grains appear to be distributed across the layered structure, suggesting the formation of a mixed composite architecture rather than a purely layered phase. HR-TEM analysis (**Figure 2(f)**) reveals clear lattice fringes with measured interplanar spacings of approximately 0.281 and 0.306 nm, which can be indexed to the (004) and (103) planes of tetragonal $CaMoO_4$-based composite, respectively. The coexistence of nanosized $CaMoO_4$-based composite grains and layered MoS_2 structures suggests the formation of interfacial contact regions and may help reduce severe restacking of the MoS_2 layers. Such structural features could contribute to increased surface exposure and interparticle interfaces that are potentially beneficial for photocatalytic surface reactions. These microscopic features indicate that MoS_2 does not simply act as a sacrificial precursor; instead, the retained layered MoS_2 phase provides a critical structural support that accommodates the in-situ growth of $CaMoO_4$-based composite nanograins and facilitates the formation of active interparticle contact zones.

Overall, the XRD-derived phase evolution is further supported by TEM/HR-TEM, SAED, and SEM observations. The formation of crystalline $CaMoO_4$-based composite is evidenced by the clear lattice fringes,

polycrystalline ring features, and the morphological transition from aggregated precursor domains to porous granular architectures. These results consistently support the proposed in situ transformation pathway induced by microwave-hydrothermal treatment. Although detailed quantitative structural refinement was not performed, the combined microscopic and diffraction analyses provide complementary evidence for the successful formation of crystalline $CaMoO_4$-based composite during the in-situ transformation process.

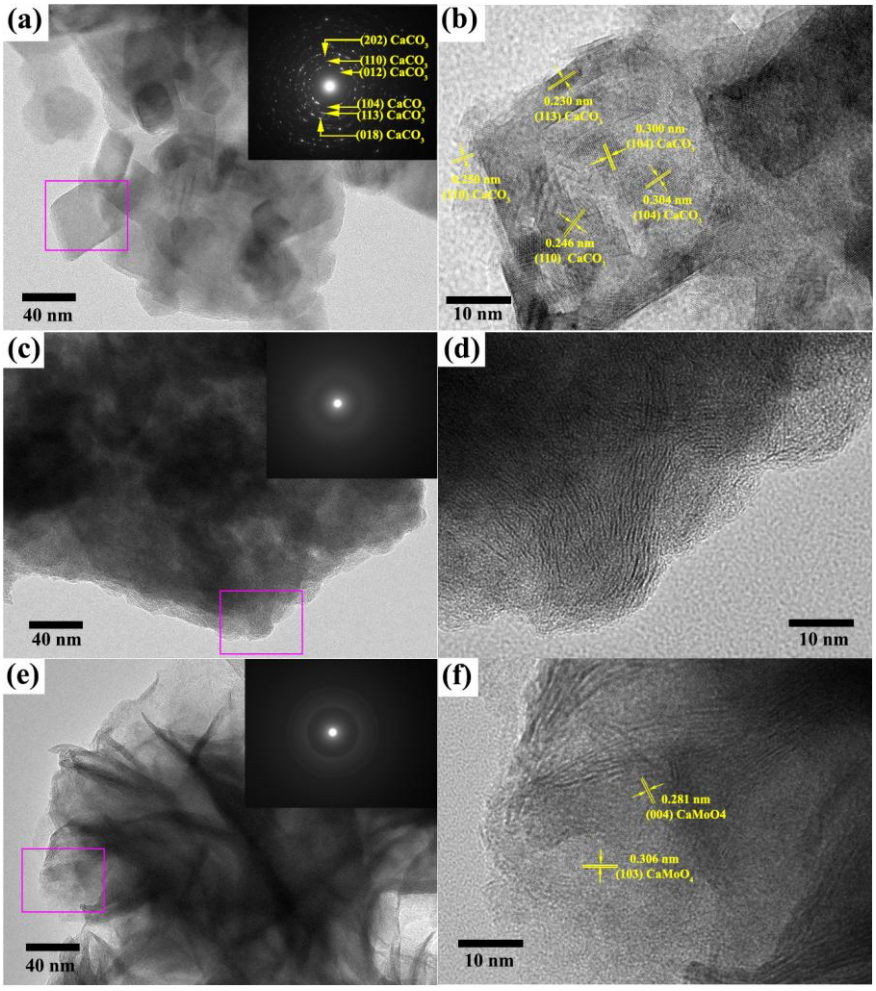


Figure 2 BF-TEM and HR-TEM image and SAED images of (a,b) $CaCO_3$, (c,d) MoS_2 and (e,f) 7 wt% $CaMoO_4$-based composites. The BE-TEM micrographs illustrate the morphological integration of the synthesized nanoscale domain with distinct interfacial contact. The high-resolution TEM lattice fringe profiles confirm the crystalline structures, indicating a prominent d-spacing of 0.36 nm corresponding to the (103) crystal plane of tetragonal $CaMoO_4$-based composite alongside facets of $CaCO_3$ and MoS_2. The inserted SAED patterns display multiple concentric rings and diffraction spots, matching the d-spacings and revealing the highly crystalline, multiple phase hybrid structure of material.

The surface morphology of $CaCO_3$, MoS_2, and the 7 wt% $CaMoO_4$-based composite at 2 magnifications was examined using SEM after sputter-coating with a thin gold layer to improve electrical conductivity and suppress charging effects under the electron beam, For $CaCO_3$, the structure consists of irregular, densely packed agglomerates formed by submicron particles (**Figures 3(a) - 3(b)**). At higher magnification, the agglomerates appear as clusters of fine grains with rough surfaces and multiple contact points between neighboring particles. In contrast, MoS_2 shows a platelet-like morphology of stacked flake aggregates, while the higher magnification image highlights large, relatively flat plates with edges, consistent with restacked nanosheets (**Figures 3(c) - 3(d)**). For the 7 wt% $CaMoO_4$-based composite, the morphology

changes markedly to a more porous, cauliflower-like agglomerate built from many nanosized particles (**Figures 3(e) - 3(f)**). Compared with $CaCO_3$ and MoS_2, the surface appears much more textured and granular at the 200 nm scale, indicating the formation of finer building blocks and a higher density of interparticle voids, which is beneficial for mass transfer during the remediation process. The interconnected and aggregated nature of the 3-dimensional cauliflower-like structures made it difficult to distinguish individual particles. Therefore, an accurate statistical analysis of particle size distribution could not be performed.

The variation in $CaCO_3$ content appears to influence the morphological evolution during the in situ hydrothermal synthesis. At low concentrations (0.3 - 0.5 wt%), the limited availability of Ca^{2+} may result in relatively low nucleation density, allowing the composite to retain morphology similar to the initial flake-like precursor structure. At 7 wt%, the increased precursor concentration is likely associated with the formation of interconnected $CaMoO_4$-based composite nanograin assemblies with porous cauliflower-like features (**Figures 3(e) - 3(f)**). Such structural evolution may contribute to a larger interfacial area and increased surface-active sites. In contrast, further increasing the loading to 10 wt% appears to promote particle aggregation and partial collapse of the porous structure, possibly due to excessive crystal growth. These observations are generally consistent with previous reports on molybdate-based composite systems synthesized under hydrothermal conditions [33,34].

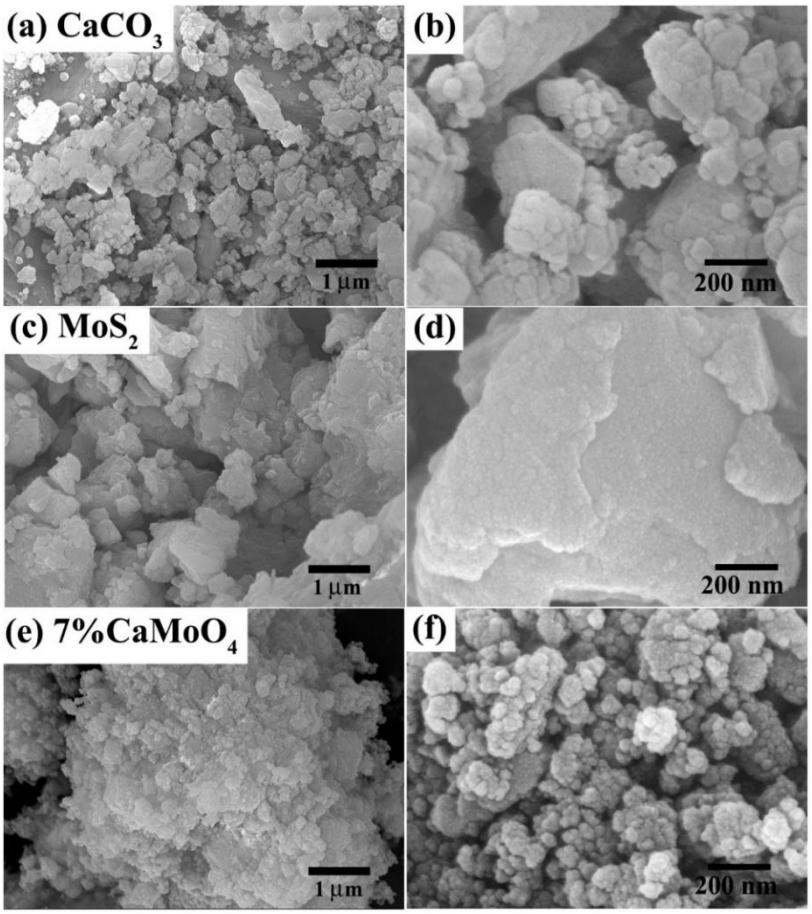


Figure 3 SEM and higher magnification images of (a,b) $CaCO_3$, (c,d) MoS_2 and (e,f) 7 wt% $CaMoO_4$-based composites.

To confirm morphological and compositional homogeneity, **Figures 4(a) - 4(g)**, shows SEM image of the 7 wt% $CaMoO_4$-based composite s together with the matching EDS element maps. In the SEM image, several microns-sized primary particles are grouped together in a rough, hierarchical texture. The EDS maps indicate that the key elements of Mo, S, Ca, C, and O are widely distributed throughout the analyzed area. The relatively uniform distribution of Ca, Mo, and O signals indicates the formation of $CaMoO_4$-based composite across the

analyzed region, with no evidence of significant elemental segregation.

The EDS sum spectrum confirms the elemental composition by showing characteristic peaks from Ca, Mo, O, S, C and Au signal is expected because the SEM sample was gold-coated to improve electrical conductivity and reduce charging. Therefore, the 7 wt% $CaMoO_4$-based composite s forms a rough agglomerate with a relatively homogeneous elemental distribution that is assembled from nanoparticles. This suggests that the constituent phases appear to be uniformly distributed at the microscale, which may contribute to more consistent catalytic or photocatalytic behavior.

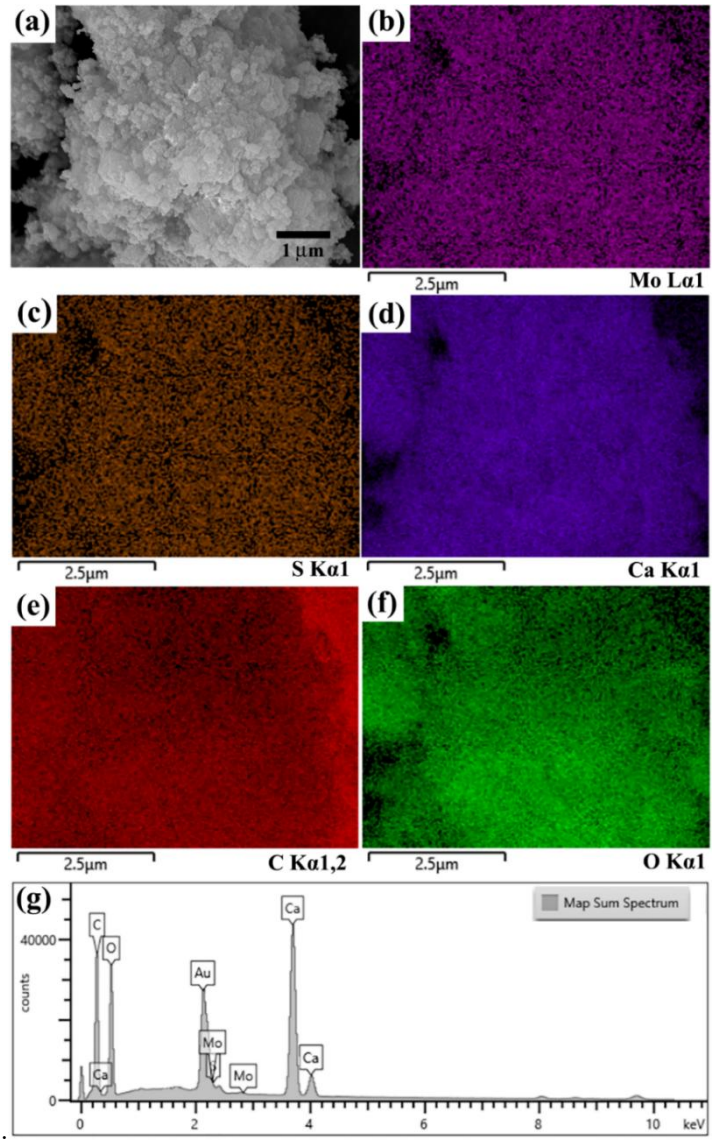


Figure 4 Microstructural and elemental mapping analysis of 7% $CaMoO_4$-based composite (a) SEM image with related elemental maps of (b) molybdenum (Mo), (c) sulfur (S), (d) calcium (Ca), (e) carbon (C), (f) oxygen (O), and (g) the corresponding quantitative EDS spectrum.

The FT-IR spectra as shown in **Figure 5** provide evidence of the in-situ transformation from the initial precursors into the $CaMoO_4$-based composite. The pure $CaCO_3$ precursor exhibited sharp and intense characteristic bands of the calcite phase at 1416 cm^{-1} (asymmetric stretch), 874 cm^{-1} (out-of-plane bending), and 712 cm^{-1} (in-plane bending). For the MoS_2 precursor, several peaks were observed at 679, 932, and 1170 cm^{-1}, attributed to the Mo−O, Mo=O, and S=O stretching modes, respectively, indicating surface oxidation and defect sites on the nanosheets [35-38].

Upon the formation of the 7 wt% $CaMoO_4$-based composite, a significant spectral evolution occurred. The sharp peaks of $CaCO_3$ and MoS_2 were noticeably broadened and overlapped by a dominant absorption band in the 400 - 900 cm^{-1} regions. This broad hill-like baseline is a signature of the stretching vibrations of MoO_4^{2-} tetrahedra within the scheelite crystal lattice. Specifically, the peak at 874 cm^{-1} became wider and merged with the Mo−O vibrations, confirming the chemical integration of Ca^{2+} and molybdate species. This shift proves that the precursors successfully transformed into a stable $CaMoO_4$-based composite phase rather than remaining as a simple physical mixture. A detailed analysis of the fingerprint region (1500 - 400 cm^{-1}) provides information on the surface functional groups and their possible relationship with the remediation performance. In the spectrum of the pristine 7 wt% $CaMoO_4$-based composite, the intensity of the asymmetric C−O stretching band associated with $CaCO_3$ at 1416 cm^{-1} is reduced compared with that of the raw precursor, which is consistent with the partial consumption of $CaCO_3$ during the in-situ phase transformation.

After the remediation processes, several changes in the fingerprint region are observed. In particular, the absorption bands associated with Mo−O stretching vibrations of MoO_4^{2-} units in the 400 - 900 cm^{-1} region show slight intensity variation and peak shifting/splitting after treatment with organic dyes (MB/MO/$CaMoO_4$) and heavy metals (Pb/Cr/$CaMoO_4$). These changes may indicate interactions between the surface molybdate species and the adsorbed pollutants through surface complexation or electrostatic interactions. In addition, the weakening or disappearance of the residual carbonate-related band at 1416 cm^{-1} after treatment suggests possible involvement of surface carbonate species during the remediation process. Overall, these spectral changes imply that the surface functional groups of the composite may contribute to the observed pollutant removal behavior.

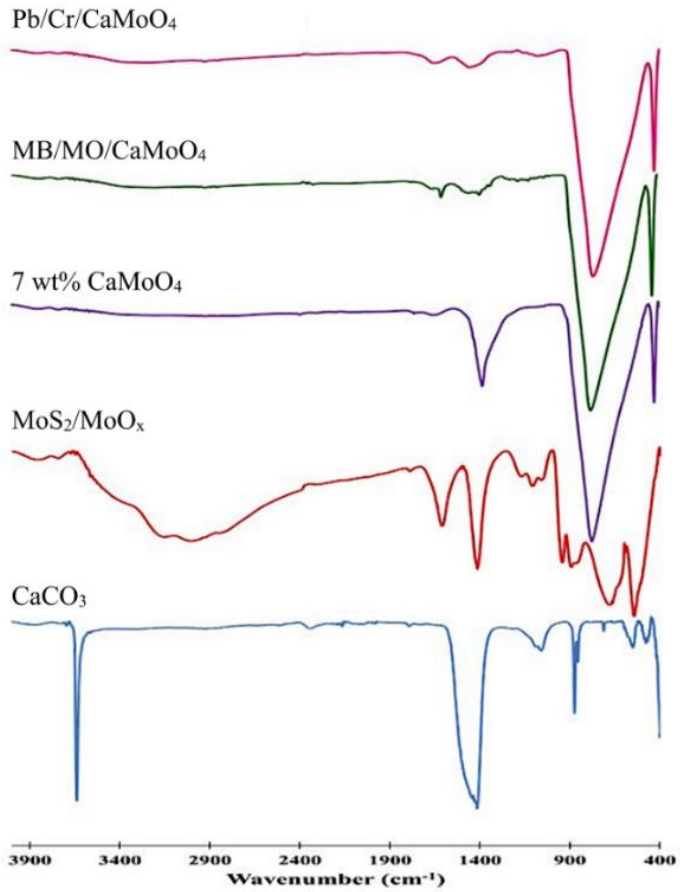


Figure 5 FT-IR of $CaCO_3$, MoS_2, 7 wt% $CaMoO_4$-based composite, MB/MO/7 wt% $CaMoO_4$-based composite (after treated) and Pb(II)/Cr(VI)/7 wt% $CaMoO_4$-based composite (after treated).

The BET specific surface area of the MoS_2/MoO_x nanosheets was found to be approximately 36.0 $m^2 g^{-1}$. Upon the in-situ formation of $CaMoO_4$-based composite, the specific surface area significantly increased to 57.5, 69.6, 73.4, and 85.5 $m^2 g^{-1}$ with the incorporation of 0.3, 0.5, 5, and 7 wt% eggshell-derived $CaCO_3$ precursors, respectively. This substantial enhancement is primarily attributed to the formation of the hierarchical, porous cauliflower-like structure, which provides a higher density of interparticle voids. Based on the structural architecture observed in the high-magnification SEM and TEM images, these aggregated nanoparticles form a network of interconnected interparticle voids. Such features are highly characteristic of mesoporous materials, where the pore sizes characteristically fall within the IUPAC mesoporous range (2 - 50 nm). This porous nature may facilitate accessible pathways for liquid-phase molecules, thereby improving mass transfer during the remediation process. Furthermore, this increase in specific surface area highlights the synergistic structural role between the MoS_2 matrix and $CaMoO_4$-based composite. The presence of MoS_2 effectively prevents the uncontrolled sintering of the growing molybdate phase, yielding a more accessible porous architecture with a higher density of surface sites. However, a further increase to 10 wt% $CaMoO_4$-based composite loading resulted in a decrease in the surface area to 30.3 $m^2 g^{-1}$, which is likely due to excessive particle agglomeration that blocked the available pores.

Photocatalytic and adsorption performance

Dyes and heavy metals removal

The photocatalytic activity of $CaCO_3$, MoS_2/MoO_x, and the $CaMoO_4$-based composite was investigated for the removal of synthetic dyes (MB and MO) and heavy metal ions (Pb(II) and Cr(VI)) under visible light illumination. In dark conditions, a significant reduction of dye concentration was observed for 5, 7, and 10 wt% $CaMoO_4$-based composite, indicating a strong physical adsorption mechanism. In contrast, low loading levels of $CaMoO_4$-based composite (0.3-0.5% $CaCO_3$) showed a slight change in dark conditions, suggesting lower adsorption capacity. Upon light illumination, the removal efficiency markedly increased due to the photo-charge carriers generated within the $CaMoO_4$-based composite. As shown in **Figures 6(a) - 6(b)**, 7 wt% $CaMoO_4$-based composite exhibited the highest photocatalytic degradation of both MB and MO compared to MoS_2/MoO_x. However, the degradation efficiency tended to decrease when $CaCO_3$ loading increased further from 7 wt%, likely due to the partial blockage of active photocatalytic sites by excessive $CaCO_3$. Thus, the 7 wt% loading was identified as the optimal dosage for MB and MO removal at 210 and 270 min, respectively. Furthermore, the high adsorption behavior of 10 wt% $CaMoO_4$-based composite helps to remove Pb(II) by 39.7% within 210 min, while the 7 wt% $CaMoO_4$-based composite achieved Cr(VI) removal by 54.8% within 180 min (**Figures 6(c) - 6(d)**). These results suggest that the higher content of $CaCO_3$ loaded under dark conditions refers to the dye adsorption behavior on the catalyst surface, while the photocatalytic reaction would undergo under light illumination, which is driven by the MoS_2-integrated system. These experiments demonstrate that both dye adsorption and photocatalysis processes are needed for the effective degradation of pollutants.

Although pure $CaMoO_4$-based composite is active only under UV light due to its wide band gap, the 7 wt% $CaMoO_4$-based composite exhibits enhanced activity under visible and solar light. This improvement is mainly due to the presence of the MoS_2 matrix, which has a narrow band gap and absorbs visible light effectively. Under light irradiation, electrons are excited in the MoS_2 phase and then transfer to the conduction band of $CaMoO_4$-based composite through the composite interface. Additionally, the in-situ synthesis helps create good contact between the 2 materials, which may facilitate charge separation and suppress recombination. Therefore, the combined effects of visible-light absorption by MoS_2 and interfacial charge transfer contribute to the improved utilization of solar energy by the composite.

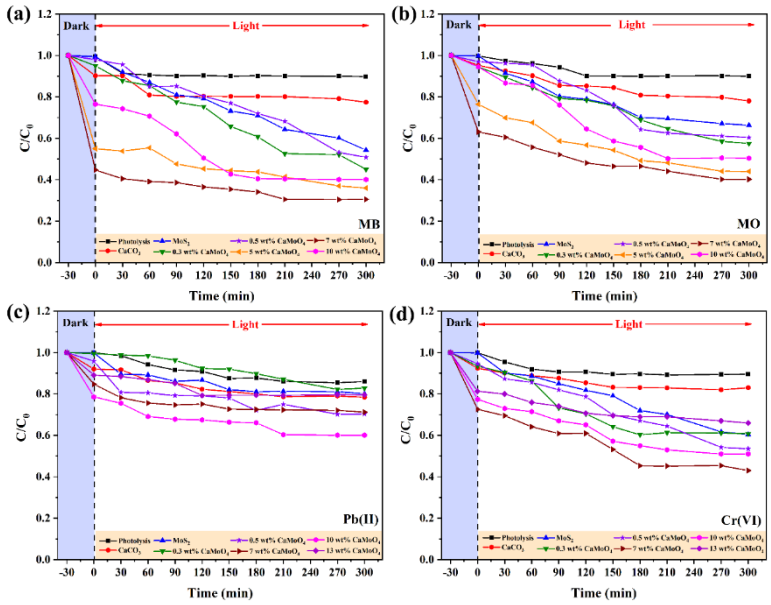


Figure 6 Removal efficiency of (a) MB, (b) MO, (c) Pb(II), and (d) Cr(VI) using different $CaMoO_4$-based composite ratios.

Effect of pH on remediation efficiency

The pH of the solution played a crucial role in influencing the surface charge and removal kinetics. To enhance removal efficiency and reduce treatment time, the same procedure with the variation of pH matrix was investigated. In this study, cationic MB dye shows an increase in adsorption as the pH tends towards neutral conditions. With the increasing surface area of the composite catalyst, $CaMoO_4$-based composite **(**with a negative potential of −40.3 mV) shows greater affinity towards cationic MB dye (+23 mV). In contrast, composite catalysts exhibit less adsorption towards MO (−16 mV). The 7 wt% $CaMoO_4$-based composite was highly effective in reducing the treatment time from 210 to 90 min for MB, and 270 to 150 min for MO. From **Figure 7(a)**, MB dye reaches a maximum 85.1% adsorption at pH 6. At this pH, the surface of $CaMoO_4$-based composite interacts with the cationic MB dye through strong electrostatic attraction. However, the adsorption efficiency of MB is reduced at pH 2, since the high concentration of H^+ ions in the solution competes for the active sites on the catalyst surface, which hinders the interaction with MB molecules. For anionic MO dye, the optimal pH 2 is the proper condition to achieve 68% efficiency within 150 min (**Figure 7(b)**). This may be explained in terms of H^+ protonated from $CaCO_3$, which then acts as an electrostatic force between the negative charge of MO.

However, the efficiency for MO is still limited because the protonation at very low pH might affect the stability of the $CaMoO_4$-based composite structure. Moreover, due to the behavior of $CaMoO_4$-based composite in certain aqueous media, molybdate $[MoO_4]^{2-}$ species can be released during the reaction, leading to a repulsive interaction with anionic MO molecules, which inhibits the overall adsorption ability [39].

For heavy metal adsorption, pH is one of the key factors influencing the adsorption efficiency due to its relationship with the surface charge of the adsorbent. From the results, the effectiveness of metal removal is significantly affected by pH; however, the pH did not influence the overall treatment time. From **Figure 7(c)**, 51.9% Pb(II) removal was achieved at pH 6 within 210 min by 10 wt% $CaMoO_4$-based composite. The removal efficiency drastically decreased at a pH lower than 3, with only 8.3% removal at 300 min. This can be explained by the surface charge of the adsorbent. At lower pH, protonation occurs, resulting in a high concentration of H^+/H_3O^+ ions in solution. These positively charged species compete with Pb(II) for the active sites on the $CaMoO_4$-based composite surface, thereby inhibiting the adsorption capacity. On the contrary, at pH 4 - 7, the ion competition diminished, possibly due to the buffering effect of $CaCO_3$, which facilitated the increase in adsorption [40]. Notably, at

pH values higher than 7, Pb(II) ions tend to precipitate as hydroxides; therefore, to minimize the contribution of bulk hydroxide precipitation and better evaluate the adsorption, photocatalytic/photoreduction removal behavior, the experiments were controlled at pH values below 7. Cr(VI) reached a removal efficiency of 65.9% within 180 min at pH 6, as illustrated in **Figure 7(d)**. The enhanced performance under this condition may be associated with photocatalytic reduction by photogenerated electrons, in addition to electrostatic interactions.

To further discuss the possible chemical pathways involved in the photocatalytic metal removal process, the observed behavior may be interpreted based on photocatalytic reduction and solution precipitation phenomena. The relatively high remediation efficiency observed at pH 6 could be associated with favorable surface and hydrolysis conditions for the reduced metal species. Under light irradiation, photogenerated electrons may participate in the reduction of dissolved Cr(VI) species to Cr(III). At near-neutral conditions, the resulting Cr(III) ions can undergo hydrolysis and may form low-solubility chromium hydroxide species, such as $Cr(OH)_3$, on or near the catalyst surface.

In the case of Pb(II), the removal process may involve a combination of photocatalytic reduction, surface adsorption, and/or precipitation-related interactions, depending on the local surface environment. These processes could contribute to the immobilization of dissolved metal species. The observed FT-IR spectral changes after treatment and the pseudo-first-order kinetic behavior provide indirect support for the involvement of surface functional groups during the remediation process.

The adsorption efficiencies were determined from the dark-equilibrium stage prior to light irradiation, while the photocatalytic (or photoreduction for metal ions) efficiencies were calculated based on the net removal achieved during the light irradiation period until steady-state equilibrium was reached. At the optimal pH of 6, MB removal reached a total removal efficiency of 85.1%, which was primarily driven by physical adsorption (65.3%) followed by 19.8% photocatalytic degradation within 90 min. In contrast, the removal of MO at pH 2 was primarily mediated by photocatalysis (63.0% within 150 min), while adsorption remained minimal at 5.0%, resulting in a total removal efficiency of 68.0%. For the heavy metal ions at pH 6, removal during light irradiation represented the dominant contribution up to 210 min, where Pb(II) and Cr(VI) exhibited photoreduction efficiencies of 49.9% and 63.9%, respectively, while adsorption played a minor role (2.0% for both), leading to total removal efficiencies of 51.9% for Pb(II) and 65.9% for Cr(VI). The treatment performance, adsorption, photocatalysis/photoreduction, and overall pollutant removal under optimized conditions, is presented in **Table 1**.

Table 1 Comparison of adsorption, photocatalytic/photoreduction, and total removal efficiencies of different pollutants under their respective optimal conditions.

Pollutant	Optimal pH	Adsorption (%)	Photocatalytic/Photoreduction (%)	Total removal (%)
MB	6	65.3	19.8	85.1
MO	2	5.0	63.0	68.0
Pb(II)	6	2.0	49.9	51.9
Cr(VI)	6	2.0	63.9	65.9

The much higher adsorption capacity of MB compared with MO can be attributed to electrostatic attraction between the cationic MB molecules and the negatively charged catalyst surface, whereas the anionic MO experiences electrostatic repulsion under the experimental conditions. In addition, the strong hydration of the sulfonate group in MO further inhibits its adsorption onto the catalyst surface. These results suggest a pollutant-dependent differences between adsorption-dependent differences in the relative contributions of adsorption and photocatalysis within the system. This partitioning represents apparent contributions under the experimental conditions and does not exclude possible interfacial coupling between adsorption and photocatalytic processes.

For practical wastewater treatment applications, the coexistence of background ionic strength and competing ions may influence the remediation performance of the material. Although explicit salt interference tests were not conducted in this study, some insight into the potential environmental robustness of the 7 wt% $CaMoO_4$-based composite can be obtained from its surface characteristics. As evidenced by the FT-IR analysis, the composite retains a residual surface carbonate species, as indicated by the remaining FT-IR band at 1,416 cm^{-1}. In addition, the composite exhibits a highly negative zeta potential (−40.3 mV), suggesting the presence of negatively charged surface sites. Although salt-interference experiments were not performed, these surface characteristics may influence pollutant interactions, and further investigation is required to assess the effect of competing ions under practical wastewater conditions.

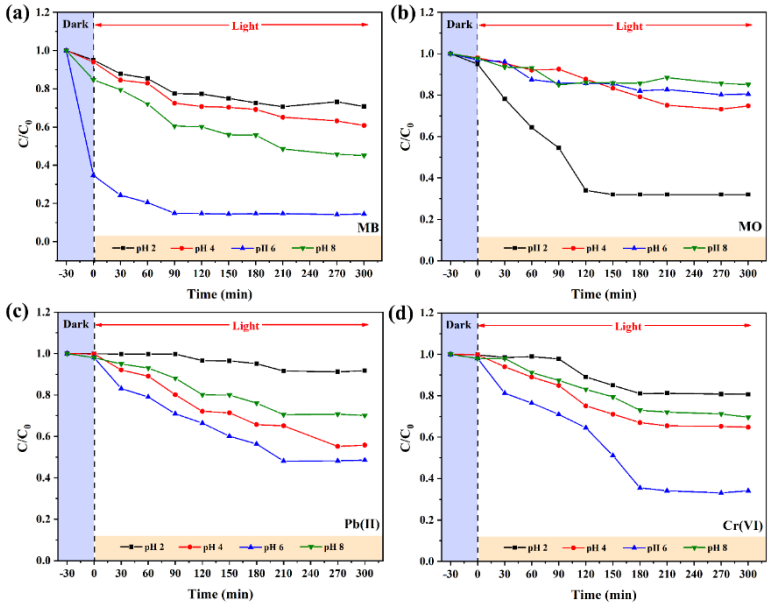


Figure 7 Removal efficiency of (a) MB, (b) MO, (c) Pb(II), and (d) Cr(VI) at different pH values.

Effect of initial concentration on remediation efficiency

To investigate the influence of initial concentration, the photocatalytic activity was evaluated at various initial concentrations ranging from 1 to 7 mg L^{-1}. The results indicated that the degradation and reduction efficiencies of $CaMoO_4$-based composite toward MB, MO, Pb(II), and Cr(VI) were significantly enhanced at lower concentrations. The decrease in initial concentration led to an improvement in removal percentages across all pollutants, while simultaneously accelerating the overall remediation process. These findings demonstrate a clear inverse correlation between initial concentration and photocatalytic efficiency, suggesting that a higher ratio of available active sites to pollutant molecules at lower concentrations facilitates a more rapid and efficient photocatalytic process.

Preliminary tests indicated that while lower concentrations (1 and 3 mg L^{-1}) achieved near-complete degradation within shorter reaction time, increasing the concentration to 7 mg L^{-1} led to a noticeable decrease in efficiency due to the shielding effect and competition for active sites. Consequently, 5 mg L^{-1} was selected as the representative concentration for detailed analysis, as it offers a balanced insight into the catalyst's performance under more challenging, realistic textile wastewater conditions (**Figure 8(a)**). Additionally, TPA analysis confirmed the generation of ·OH radicals, which are the crucial oxidative species responsible for the degradation of organic dyes (MB and MO). While these radicals facilitate the mineralization of dyes, the reduction of Pb(II) and Cr(VI) is primarily driven by the photo-generated electrons in the conduction band [41].

The proposed mechanism equation for photocatalytic degradation of MB and MO using $CaMoO_4$-based composite is outlined in Eqs. (1) - (8), while the adsorption mechanisms onto the $CaCO_3$ surface are proposed by Eqs. (9) - (12).

$$CaMoO_4 + h\nu \rightarrow e^- + h^+ \quad (1)$$

$$H_2O + h^+ \rightarrow \cdot OH + H^+ \quad (2)$$

$$O_2 + e^- \rightarrow \cdot O_2^- \quad (3)$$

$$\cdot O_2^- + H^+ \rightarrow \cdot HO_2 \quad (4)$$

$$2 \cdot HO_2 \rightarrow H_2O_2 + O_2 \quad (5)$$

$$Dye + (\cdot OH + \cdot O_2^-) \rightarrow \text{Degraded products} \quad (6)$$

$$\text{Surface-OH} + OH^- + MB^+ \leftrightarrow \text{Surface-O-MB} + H_2O \quad (7)$$

$$\text{Surface-}OH_2^+ + MO^- \leftrightarrow \text{Surface-}OH_2\text{-MO} \quad (8)$$

$$\text{Surface-}(CaCO_3) + Pb(II) \leftrightarrow [\text{Surface-}(CaCO_3)\cdots Pb(II)]_{adsorbed} \quad (9)$$

$$\text{Surface-}(CaCO_3) + Cr(VI) \leftrightarrow [\text{Surface-}(CaCO_3)\cdots Cr(VI)]_{adsorbed} \quad (10)$$

$$Pb(II) + 2e^- \rightarrow Pb^0 \quad (11)$$

$$Cr_2O_7^{2-} + 14H^+ + 6e^- \rightarrow 2Cr^{3+} + 7H_2O \quad (12)$$

Reusability and stability

The reusability of the $CaMoO_4$-based composite was evaluated through five repeated cycles. The removal efficiency for all pollutants remained relatively consistent for the first 3 cycles but showed a noticeable decline in cycles 4 and 5 (**Figure 8(b)**). A significant change in the removal capacity for both dyes and metal ions was observed starting from the fourth cycle compared to the initial stages [1,42]. During these cycles, the removal efficiencies remained approximately 66.5% - 85.1% for dyes and 50.3% - 65.9% for metal ions.

To understand this, the FT-IR spectra of $CaMoO_4$-based composite before treatment was compared with the spectra obtained after Pb(II) and Cr(VI) remediation (**Figure 5**). Before the process, $CaMoO_4$-based composite showed the characteristic (Mo-O) stretching band at 771 cm^{-1} and the calcite phase of $CaCO_3$ at 874 cm^{-1}. After the adsorption and photocatalytic treatment, the Mo-O band slightly shifted to 767 cm^{-1}. Both the molybdate and carbonate frameworks were actively involved in the interaction with the metal ions. A new peak was observed post-treatment at 1384, 1455 and 1645 cm^{-1}, while the peak at 3639 cm^{-1} (attributed to surface -OH groups) disappeared in both the dye and heavy metal remediation samples. These spectral changes provide strong evidence that these functional groups served as active sites during the adsorption and photocatalytic processes.

In conclusion, based on the sustained removal efficiency, it can be deduced that $CaMoO_4$-based composite provides high stability and robust recycling capacity for treating MB, MO, Pb(II), and Cr(VI) in aqueous matrices. Furthermore, the performance under different light sources-both synthetic and natural solar light-was validated. As expected, while the maximum removal of all pollutants under optimized conditions (pH and initial concentration) was slightly less effective under natural sunlight compared to synthetic light (**Figure 8(c)**), the results remain highly promising for practical, real-world wastewater treatment applications.

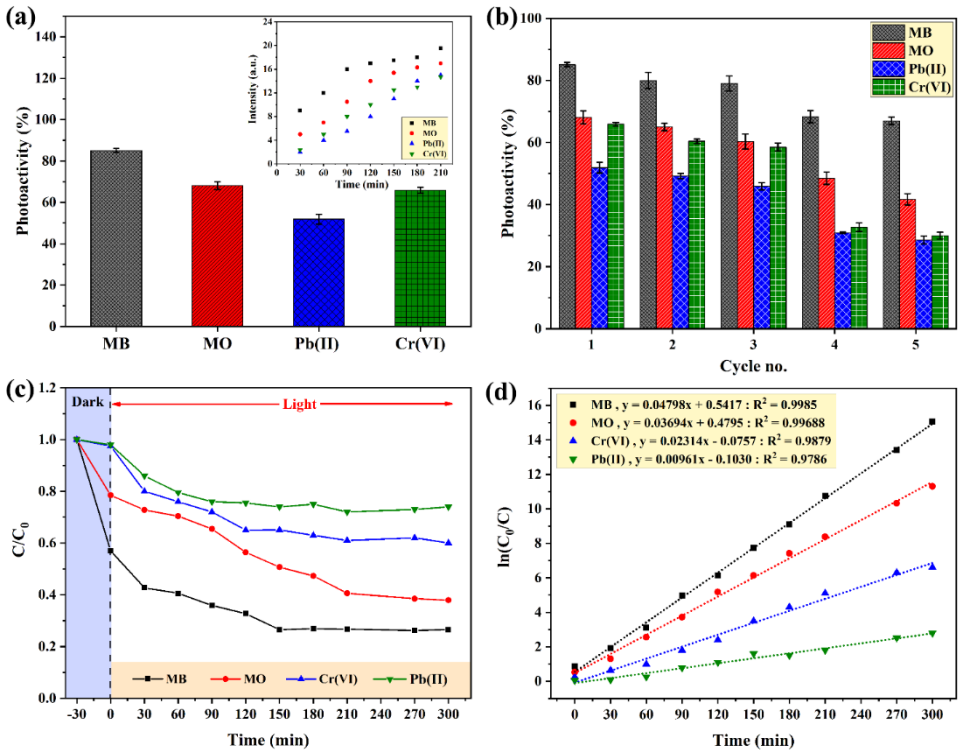


Figure 8 Effect of initial concentration on the removal efficiency of MB, MO, Pb(II), and Cr(VI) with TPA analysis (inset), (b) reusability, (c) removal efficiency under natural sunlight illumination, and (d) kinetic study.

Remediation kinetics and adsorption isotherm studies

To further evaluate the surface interaction dynamics and the distribution of adsorption sites on the synthesized heterojunction, the equilibrium data obtained from the initial concentration variations were analyzed using the Langmuir and Freundlich adsorption isotherm models (**Table 2**). The adsorption behavior shows a better fit with the Freundlich isotherm model ($R^2 > 0.95$) compared to the Langmuir model. This result suggests that the adsorption of both organic dyes and heavy metal ions occurs on a heterogeneous surface with adsorption sites of varying energies. This behavior may be associated with the porous structure of the composite, which provides a diverse distribution of surface adsorption sites.

Table 2 Adsorption isotherm parameters (Langmuir and Freundlich) for the removal of target pollutants by the 7 wt% $CaMoO_4$-based composite.

Pollutants	Langmuir			Freundlich		
	q_{max} (mg g^{-1})	K_L (L mg^{-1})	R^2	K_F	1/n	R^2
MB	11.55	0.383	0.945	3.90	0.426	0.980
MO	9.47	0.301	0.933	2.97	0.453	0.974
Cr(VI)	7.67	0.184	0.875	1.65	0.520	0.971
Pb(II)	5.82	0.125	0.911	0.97	0.585	0.959

To better understand the kinetic process of dye and metal remediation, a kinetic study was conducted to determine the rate constant (k). The linear relationship between $-\ln(C/C_0)$ and irradiation time, suggesting that the kinetic results for the photocatalytic activity and photoreduction of an aqueous MB, MO, Pb(II), and Cr(VI) solution follow pseudo-first-order kinetic reaction model. The model is expressed using the following equation:

$$-\ln(C/C_O) = kt$$

where k is the pseudo-first-order rate constant (min^{-1}), C_0 is the initial concentration of the contaminant after the dark adsorption period (mg L^{-1}), C is the concentration at different irradiation time intervals (t), and t is the irradiation time (min).

Table 3 Pseudo-first-order kinetic parameters for the removal of various pollutants by 7 wt% $CaMoO_4$-based composite composites.

Pollutants	Rate constant k, (min^{-1})	Correlation coefficient, R^2
MB	0.0480	0.9985
MO	0.0369	0.9969
Cr(VI)	0.0231	0.9880
Pb(II)	0.0096	0.9787

As illustrated in **Figure 8(d)** and **Table 3**, the $CaMoO_4$-based composite demonstrated high efficiency across all tested contaminants. The calculated rate constants for MB, MO, Cr(VI), and Pb(II) were 0.0480, 0.0369, 0.0231, and 0.0096 min^{-1}, respectively. The correlation coefficients ($R^2 > 0.95$) for all plots confirm that the experimental results are in excellent agreement with the pseudo-first-order model. These quantitative findings highlight the robust catalytic performance of 7 wt% $CaMoO_4$-based composite in treating diverse types of wastewater pollutants.

To elucidate the kinetic nature of the multi-pollutant remediation, it is important to study the distinct contributions of dark adsorption versus light-driven processes for each contaminant. As demonstrated by the experimental control, MB removal was strongly driven by surface adsorption (76.4%) with a photocatalytic contribution of 23.6%, whereas MO removal was mostly driven by active photocatalysis (92.6%) with a minimal adsorption phase (7.4%). For the heavy metal ions, the remediation processes were predominantly driven by photogenerated electron-induced reduction, with photoreduction contributing 96.1% for Pb(II) and 97.0% for Cr(VI), while physical adsorption played a minor role (3.9% and 3.0%, respectively). Therefore, a pseudo-first-order kinetic model was employed as a common framework to describe the overall remediation behavior of the investigated pollutants. The obtained correlation coefficients (R^2 = 0.9787 - 0.9985) indicate that the model provides a satisfactory description of the experimental data under the investigated conditions.

To investigate the photocatalytic mechanism, the primary active species related to the photo-degradation of MB (as a model organic dye) were studied by scavenger capturing. Benzoquinone, ammonium oxalate, and isopropanol were used as trapping agents for $\cdot O_2^-$, h^+, and ·OH, respectively. In the absence of scavengers, the photocatalytic activity of MB was 91.26%. Upon the addition of benzoquinone, ammonium oxalate, and isopropanol, the degradation efficiencies significantly decreased to 21.26%, 57.45%, and 80.17%, respectively. These results suggest that $\cdot O_2^-$ plays a dominant role in the oxidation process, while h^+ and ·OH may also contribute synergistically to the photocatalytic reaction, following the order: $\cdot O_2^- > h^+ >$ ·OH. Since the removal of Pb(II) and Cr(VI) may involve reduction by photogenerated electrons, the scavengers used for organic degradation were not applied to the heavy metal systems to avoid potential complexation interference.

The scavenger trapping experiments, which revealed the contribution order of $\cdot O_2^- > h^+ >$ ·OH, provide supportive evidence for the proposed charge-transfer mechanism of the 7 wt% $CaMoO_4$-based composite. The dominant role of $\cdot O_2^-$ radicals is consistent with the estimated conduction band edge potentials of $CaMoO_4$ (−0.50 eV) and MoS_2 (−0.08 eV), which are more negative than the reduction potential of $O_2/\cdot O_2^-$ (−0.046 eV vs. NHE). This suggests that photogenerated electrons may participate in the reduction of dissolved oxygen to form superoxide radicals.

In addition, the relatively positive valence band potential of $CaMoO_4$ (+3.00 eV) may facilitate the oxidation of adsorbed dye molecules and contribute to the generation of ·OH radicals from water or surface hydroxyl species. The consistency between the

scavenger experiments and the estimated band-edge positions supports a Type-II charge-transfer pathway, which facilitates effective charge separation within the composite system.

Total organic carbon analysis

To evaluate the mineralization capability of the $CaMoO_4$-based composite, total organic carbon (TOC) analysis was conducted. After the photocatalytic process, the TOC removal efficiency was found to be 44.65%. While this value is lower than the decolorization efficiency, it confirms that a significant portion of the MB molecules was partially mineralized into inorganic by-products such as CO_2 and H_2O. The difference between the decolorization and mineralization percentages suggests the presence of intermediate organic fragments in the solution, which require longer irradiation time for complete degradation. Nonetheless, the substantial reduction in TOC directly demonstrates the effectiveness of the synthesized catalyst in breaking down the organic backbone of the dye.

The TOC analysis suggests the mineralization of organic dyes (MB and MO), while the kinetic studies and removal efficiency data support the effective remediation of heavy metals (Pb(II) and Cr(VI)). Together, these results indicate that the synthesized catalyst can address both organic and inorganic pollutants, offering a promising approach for complex industrial wastewater treatment.

To further highlight the performance characteristics of the present system, a detailed comparison with related state-of-the-art materials is summarized in **Table 4**. Most reported materials focus on removing either organic dyes or heavy metals as their primary target. Similarly, precursor phases like $CaCO_3$ or conventional biosorbents mainly function via adsorption or ion-exchange mechanisms for heavy metal capture. In contrast, the eggshell-derived 7 wt% $CaMoO_4$-based composite exhibits effective performance toward both organic and inorganic pollutants under simulated and solar light irradiation. Although some previously reported materials achieved higher removal efficiencies for specific pollutants, they were evaluated for individual contaminants or required long treatment times. These results suggest that the developed composite may have potential for treating wastewater containing various pollutants.

Table 4 Comparison of pollutant removal efficiency with related literature.

Materials	Pollutants	Mechanism	Removal efficiency (%)	[Ref]
MoS_2	MB	Photocatalytic	98% (25 min)	[43]
	Phenolphthalein	Photocatalytic	89% (25 min)	
MoS_2	MB	Photocatalytic	98% (120 min)	[44]
Biosorbents/$CaCO_3$	Cu (II)Zn(II)Pb (II)	Ion exchange/Precipitation	80% - 100 % (60 min)	[45]
$CaCO_3$	Cd (II)	Adsorption	97% (24 h)	[46]
	Pb (II)		100% (24 h)	
$CaMoO_4$	MB	Photocatalytic	96% (60 min)	[47]
7 wt% $CaMoO_4$	MB/MO	Adsorption/Photocatalytic	68% - 85% (90 - 150 min)	This work
	Cr (VI)/Pb (II)	Adsorption/Photoreduction	52% - 66% (180 - 210 min) Under synthetic light	
	MB/MO	Adsorption/Photocatalytic	60% - 75% (5 h)	
	Cr (VI)/Pb (II)	Adsorption/Photoreduction	30% - 40% (5 h) Under solar light	

Phytotoxicity assessment of treated wastewater on *H. verticillata*

This study investigated the accumulation of Ca, Mo, Pb(II), and Cr(VI) in the aquatic macrophyte *H. verticillata* to evaluate the phytotoxicity of wastewater treated with a 7 wt% $CaMoO_4$-based composite photocatalyst. Plant tissues were analyzed using FAAS, and the results are presented in **Table 5**. To ensure analytical reliability, samples were spiked with known concentrations of the target elements, yielding high recovery rates (> 79%).

As shown in **Table 5**, Ca concentrations in plants exposed to treated wastewater (38.5 ± 3.1 and 31.8 ± 4.1 mg kg^{-1}) were notably higher than in the control groups (32.7 ± 1.5 and 25.5 ± 2.2 mg kg^{-1}. This increase is attributed to the dissolution of $CaCO_3$ and the subsequent release of Ca ions, which are readily absorbed by plant tissues [48,49]. This accumulation likely functions as a protective mechanism; according to Nazir *et al.* [50], exogenous calcium mitigates heavy metal toxicity by regulating ion transport and enhancing cell wall characteristics. The competitive interaction between Ca(II) and divalent metal ions such as Pb(II) and Cr(VI) potentially limited their bioaccumulation, as evidenced by the low metal concentrations detected in the treated groups. The concentrations of Mo, Pb(II), and Cr(VI) were below the detection limit (ND) in all control samples. Following 30 days of exposure to treated wastewater, these elements were detected in plant tissues at low levels: Mo (2.64 - 4.30 mg kg^{-1}), Pb(II) (0.04 - 0.07 mg kg^{-1}), and Cr(VI) (0.02 - 0.03 mg kg^{-1}). While the treatment did not completely prevent trace element accumulation, the observed levels remained well below established phytotoxicity thresholds. Molybdenum concentrations were within the safe range (< 10 mg kg^{-1}), and Pb and Cr levels were far below the toxic limits of 30 - 50 and 5 - 10 mg kg^{-1}, respectively [51,52]. Following a 30-day exposure to the treated wastewater, the detected concentrations of Mo, Pb(II), and Cr(VI) in the plant tissue remained significantly low. Based on established phytotoxicity thresholds, these observed concentrations are unlikely to cause significant phytotoxicity to *H. verticillata*. According to the International Molybdenum Association [53], referencing Gupta [54], while molybdenum is essential for plant metabolism, excessive accumulation can interfere with enzyme activities. In this study, Mo concentrations remained within the safe range, well below the typical toxicity threshold of 10 mg kg^{-1}.

Likewise, Pb concentrations above 30 - 50 mg kg^{-1} in plant tissues are generally considered toxic, causing growth inhibition and metabolic disruption [51] Chromium also becomes phytotoxic when its concentration exceeds 5 - 10 mg kg^{-1}, resulting in reduced chlorophyll synthesis and root growth inhibition [52]. In this study, the concentrations of Pb(II) and Cr(VI) were extremely low, suggesting that the photocatalytic process induces minimal metal-induced stress. These findings confirm that photocatalytic treatment with $CaMoO_4$-based composite is a promising approach for wastewater remediation, as it does not induce significant phytotoxic effects on *H. verticillata* under the tested conditions. Further investigations are recommended to evaluate the long-term effects of chronic exposure to these low concentrations.

Table 5 FAAS analysis of *H. verticillate*.

Elements	Plant treatments with 7 wt% $CaMoO_4$-based composites			
	Control (mg kg^{-1})	Sample site 1 (mg kg^{-1})	Control (mg kg^{-1})	Sample site 2 (mg kg^{-1})
Ca	32.7 ± 1.5	38.5 ± 3.1	25.5 ± 2.2	31.8 ± 4.1
Mo	ND	4.30 ± 6.2	ND	2.64 ± 1.7
Pb(II)	ND	0.07 ± 4.8	ND	0.04 ± 3.5
Cr(VI)	ND	0.03 ± 5.6	ND	0.02 ± 4.8

Detection limit of Ca(II), Mo, Pb(II), Cr(VI) was 0.015, 0.15, 0.15 and 0.03 mg L^{-1}, respectively.

Conclusions

The $CaMoO_4$-based composites, synthesized via a rapid microwave-hydrothermal route using eggshell-derived precursors, exhibited exceptional performance in the simultaneous removal of organic dyes and heavy metals. The synergistic integration of surface adsorption and visible-light photocatalysis demonstrated high efficacy in photodegrading MB and MO, while effectively removing Pb(II) and Cr(VI). Under optimized conditions with visible light irradiation, the removal efficiencies reached 85.1% (90 min) for MB, 68.1% (150 min) for MO, 51.9% (210 min) for Pb(II), and 65.9% (210 min) for Cr(VI). Under natural sunlight, the composite maintained substantial activity, achieving removal efficiencies of approximately 75% (MB), 60% (MO), 30% (Pb(II)), and 40% (Cr(VI)) within a 5 h exposure period. These results confirm that the combined adsorption-photocatalysis mechanism is highly effective for pollutant remediation. Furthermore, the $CaMoO_4$-based composite offers an environmentally compatible approach for wastewater remediation without inducing significant phytotoxic effects in *H. verticillata*. The release of Ca^{2+} from the catalyst was found to mitigate heavy metal stress by reducing metal uptake in plant tissues, suggesting its suitability for safe and sustainable environmental applications. Overall, the synthesized $CaMoO_4$-based composite demonstrates great potential for the treatment of textile wastewater both under solar or synthetic visible-light irradiation.

Acknowledgements

This research project is supported by Nakhon Sawan Rajabhat University, Thailand (Fundamental Fund: fiscal year 2023 by National Science Research and Innovation Fund (NSRF)) 4120856 (2566A13712001).

Declaration of generative AI in scientific writing

Generative AI was used to refine language and improve readability. The authors have reviewed and edited the output and assume full responsibility for the final content.

CRediT Author Statement

Chonlada Dechakiatkrai Theerakarunwong: Conceptualization, Methodology, Supervision, Validation, Data curation, Formal analysis, Funding acquisition, and Writing – original draft. **Waraporn Chuaychai:** Formal analysis and Writing – review & editing. **Rutairat Photi:** Writing – review & editing. **Chaikarn Leawhiran:** Conceptualization, Validation, Writing – review & editing.

References

[1] AM Aljeboree, HH Ghazi, SA Hussein, MA Jawad, SA Khuder and AF Alkaim. Facile fabrication of a low-cost carboxymethyl cellulose-polyacrylamide composite for the highly efficient removal of cationic dye: Optimization, kinetic and reusability. *Journal of the Iranian Chemical Society* 2025; **22(1)**, 91-111.

[2] AM Aljeboree, AF Alkaim, SA Hussein, FH Alsultany and MA Jawad. Ecofriendly k-carrageenan-based hydrogel with strong adsorption and higher abilities to remove crystal violet from aqueous solution: Thermodynamic, isotherm and kinetic investigation. *Journal of Inorganic and Organometallic Polymers and Materials* 2025; **35(4)**, 2921-2942.

[3] L Saya, V Malik, A Singh, S Singh, G Gambhir, WR Singh, R Chandra and S Hooda. Guar gum based nanocomposites: Role in water purification through efficient removal of dyes and metal ions. *Carbohydrate Polymers* 2021; **261**, 117851.

[4] T Shi, Z Xie, X Mo, Y Feng, T Peng and D Song. Highly efficient adsorption of heavy metals and cationic dyes by smart functionalized sodium alginate hydrogels. *Gels* 2022; **8(6)**, 343.

[5] S Ahmed, S Aktar, S Zaman, RA Jahan and ML Bari. Use of natural bio-sorbent in removing dye, heavy metal and antibiotic-resistant bacteria from industrial wastewater. *Applied Water Science* 2020; **10(5)**, 107.

[6] TM Kathawala, KV Gayathri and PS Kumar. A performance comparison of anaerobic and an integrated anaerobic-aerobic biological reactor system for the effective treatment of textile wastewater. *International Journal of Chemical Engineering* 2021; **2021**, 8894332.

[7] K Paździor, L Bilińska and S Ledakowicz. A review of the existing and emerging technologies in the combination of AOPs and biological processes in industrial textile wastewater treatment. *Chemical Engineering Journal* 2019; **376**, 120597.

[8] M Tabish, AB Tabinda, Z Mazhar, A Yasar, J Ansar and I Wasif. Physical, chemical and biological treatment of textile wastewater for removal of dyes and heavy metals. *Desalination and Water Treatment* 2024; **320**, 100842.

[9] G Chandrabose, A Dey, SS Gaur, S Pitchaimuthu, H Jagadeesan, NSJ Braithwaite, V Selvaraj, V Kumar and S Krishnamurthy. Removal and degradation of mixed dye pollutants by integrated adsorption-photocatalysis technique using 2-D MoS_2/TiO_2. *Chemosphere* 2021; **279**, 130467.

[10] Y Cao, K Wang, P Zhu, X Zou, G Ma, W Zhang, D Wang, J Wan, Y Ma, X Sun and J Dong. A near-infrared triggered upconversion/MoS_2 nanoplatform for tumour-targeted chemo-photodynamic combination therapy. *Colloids and Surfaces B: Biointerfaces* 2022; **213**, 112393.

[11] PP Singh, S Sinha, G Pandey and V Srivastava. Molybdenum disulfide (MoS_2) based photoredox catalysis in chemical transformations. *RSC Advances* 2022; **12(46)**, 29826-29839.

[12] B Balan, MM Xavier and S Mathew. MoS_2-based nanocompositess for photocatalytic hydrogen evolution and carbon dioxide reduction. *ACS Omega* 2023; **8(29)**, 25649-25673.

[13] X Li, J Wan, Y Tang, C Wang, Y Zhang, D Lv, M Guo, Y Ma and Y Yang. Boosting the UV-vis-NIR photodetection performance of MoS_2 through the cavity enhancement effect and bulk heterojunction strategy. *ACS Applied Materials & Interfaces* 2024; **16(22)**, 29003-29015.

[14] A Rahman, JR Jennings, AL Tan and MM Khan. Molybdenum disulfide-based nanomaterials for visible-light-induced photocatalysis. *ACS Omega* 2022; **7**, 22089-22110.

[15] N Ahmad, M Javed, MA Qamar, U Kiran, S Shahid, MB Akbar, M Sher and A Amjad. Synthesis, characterization and potential applications of Ag@ZnO nanoparticles with S@g-C_3N_4. *Advanced Materials Research* 2022; **11(3)**, 225-235.

[16] M Baláž, EV Boldyreva, D Rybin, S Pavlovic, D Rodríguez-Padrón, T Mudrinic and R Luque. State-of-the-art of eggshell waste in materials science: Recent advances in catalysis, pharmaceutical applications, and mechanochemistry. *Frontiers in Bioengineering and Biotechnology* 2021; **8**, 612567.

[17] S Das, PK Mohanty and BK Mallik. Agricultural and pharmaceutical applications of eggshells: A comprehensive review of eggshell waste value-added products. *Journal of Pharmaceutical Negative Results* 2022; **13(8)**, 3979-3984.

[18] RO Zonato, BR Estevam, ID Perez, VAS Ribeiro and RF Boina. Eggshell as an adsorbent for removing dyes and metallic ions in aqueous solutions. *Cleaner Chemical Engineering* 2022; **2**, 100023.

[19] TGS Meydan, SS Moosavi, Z Sabouri and M Darroudi. Green synthesis of $CaCO_3$ nanoparticles for photocatalysis and cytotoxicity. *Bioprocess and Biosystems Engineering* 2023; **46**, 727-734.

[20] MN Mazlee and H Zunairah. Science mapping of catalyst support for gas adsorption applications. *Advanced Materials Research* 2024; **13(3)**, 203-210.

[21] O Eskikaya, M Gun, R Bouchareb, Z Bilici, N Dizge, R Ramaraj and D Balakrishnan. Photocatalytic activity of calcined chicken eggshells for Safranin and Reactive Red 180 decolorization. *Chemosphere* 2022; **304**, 135210.

[22] A Manyatshe and LL Sibali. A review on egg waste-based adsorbents for the removal of organic and inorganic contaminants from aqueous solution. *Heliyon* 2025; **11**, e42278.

[23] A Amarasinghe and D Wanniarachchi. Eco-friendly photocatalyst derived from egg shell waste for dye degradation. *Journal of Chemistry* 2019; **2019**, 8184732.

[24] S Ummartyotin and H Manuspiya. A critical review of eggshell waste: An effective source of hydroxyapatite as photocatalyst. *Journal of Metals, Materials and Minerals* 2018; **28(1)**, 124-135.

[25] QS Zhou, WT Yun, JT Xi, XB Li, TG Qi, GH Liu and ZH Peng. Molybdenite-limestone oxidizing roasting followed by calcine leaching with ammonium carbonate solution. *Transactions of*

Nonferrous Metals Society of China 2017; **27(7)**, 1618-1626.

[26] J Wang, S Sun, L Pan, Z Xu, H Ding and W Li. Preparation and properties of $CaCO_3$-supported nano-TiO_2 composite with improved photocatalytic performance materials. *Materials* 2019; **12**, 3369.

[27] C Liu, C Huang, C Hu, D Wang, Y Zhong and C Tang. $CaCO_3/BiO_{2-x}$/CdS composite with rapid photocatalytic reduction of Cr(VI) under visible light. *Nanomaterials* 2026; **16**, 376.

[28] H Zhang, XY Gong, WX Li, XH Ma, CY Tang and ZL Xu. Thin-film membranes containing tannic acid-Fe^{3+} modified MoS_2 nanosheets with enhanced nanofiltration performance. *Journal of Membrane Science* 2020; **611**, 118605.

[29] M Minakshi, AJ Barlow, DRG Mitchell, C Baur, J Chable, M Fichtner, A Banerjee, S Chakraborty and R Ahuja. Phase evolution in calcium molybdate nanoparticles as a function of synthesis temperature and its electrochemical effect on energy storage. *Nanoscale Advances* 2019; **1**, 565.

[30] X Zhang, J Huang, Z Kang, DP Yang and R Luque. Eggshell-templated synthesis of PbS/$CaCO_3$ nanocomposites for CO_3^- mediated efficient degradation of tetracycline under solar light irradiation. *Journal of Molecular Catalysis A: Chemical* 2020; **484**, 110786.

[31] DA Yaseen and M Scholz. Textile dye wastewater characteristics and constituents of synthetic effluents: A critical review. *International Journal of Environmental Science and Technology* 2019; **16(2)**, 1193-1226.

[32] AM Nasib, S Simon, SM Rasidi, SKE Ab Rahim, HP Yong, NQ Hwa and K Johari. Coagulant bath medium effect towards polylactic acid membranes structure and methylene blue dye removal. *Advanced Materials Research* 2024; **13(3)**, 243-251.

[33] W Wang, Y Hu, J Goebl, Z Lu, L Zhen and Y Yin. Shape- and size-controlled synthesis of calcium molybdate doughnut-shaped microstructures. *Journal of Physical Chemistry C* 2009; **113**, 16414-16423.

[34] M Laguna, NO Nuñez, AI Becerro and M Ocaña. Morphology control of uniform $CaMoO_4$ microarchitectures and development of white light emitting phosphors by Ln doping (Ln = $Dy3^+$, Eu^{3+}). *CrystEngComm* 2017; **19**, 1590.

[35] E Fosso-Kankeu, M Spiro, FB Waanders, N Kumar and SS Ray. Hydrothermal synthesis, characterization and adsorption testing of MoS_2-zeolite for the removal of lead in an aqueous solution. *In*: Proceedings of the 10th International Conference on Advances in Science, Engineering and Technology for Healthcare, Cape Town, South Africa. 2018.

[36] DS Mallya, G Yang, W Lei, S Muthukumaran and K Baskaran. Functionalized MoS_2 nanosheets enabled nanofiltration membrane with enhanced permeance and fouling resistance. *Environmental Technology & Innovation* 2022; **27**, 102719.

[37] GB Cai, SF Chen, L Liu, J Jiang, HB Yao, AW Xu and HS Yu. 1,3-Diamino-2-hydroxypropane-N,N,N′,N′-tetraacetic acid stabilized amorphous calcium carbonate: Nucleation, transformation and crystal growth. *CrystEngComm* 2010; **12(1)**, 234-241.

[38] DJ Silva and H Wiebeck. ATR-FTIR spectroscopy combined with chemometric methods for the classification of polyethylene residues containing different contaminants. *Journal of Polymers and the Environment* 2020; **30(7)**, 3031-3044.

[39] S Roobakhsh, Z Rostami and S Azizian. Can MoS_2 nanosheets be used as adsorbent for water treatment? *Separation and Purification Technology* 2018; **200**, 23-28.

[40] Y He, X Jia, S Zhou, J Chen, S Zhang, X Li, Y Huang, T Wagberg and G Hu. Separatable MoS_2 loaded biochar/$CaCO_3$/Alginate gel beads for selective and efficient removal of Pb(II) from aqueous solution. *Separation and Purification Technology* 2022; **303**, 122212.

[41] CD Theerakarunwong, O Kaewthet and S Phanichphant. Potential effectiveness of visible-light-driven Fe/TiO_2 photocatalysts for degradation of dyes contaminated wastewater and their antibacterial activity. *ScienceAsia* 2023; **49**, 454-461.

[42] LO Amaral and AL Daniel-da-Silva. MoS_2 and MoS_2 for adsorption and photodegradation of water pollutants: A review. *Molecules* 2022; **27(20)**, 6782.

[43] D Nayak, A Kumar and R Thangavel. Synthesis of MoS_2 nanoflowers for photocatalytic degradation of organic dyes. *ACS Applied Nano Materials* 2023; **6**, 19476-19490.

[44] MTL Lai, KM Lee, TC K Yang, GT Pan, CW Lai, CY Chen, MR Johan and JC Juan. The improved photocatalytic activity of highly expanded MoS_2 under visible light emitting diodes. *Nanoscale Advances* 2024; **3**, 1106.

[45] S Wierzba, J Makuchowska-Fryc, A Kłos, Z Ziembik and W Ochędzan-Siodłak. Role of calcium carbonate in the process of heavy metal biosorption from solutions: Synergy of metal removal mechanisms. *Scientific Reports* 2022; **12**, 17668.

[46] R Liu, Y Guan, L Chen and B Lian, Adsorption and desorption characteristics of Cd^{2+} and Pb^{2+} by micro and nano-sized biogenic $CaCO_3$. *Frontiers in Microbiology* 2018; **9**, 41.

[47] Y Xu, Y Han, R Zhao, J Han and L Wang. CdSe-decorated flower like $CaMoO_4$ microspheres with enhanced hydrogen production activity. *Langmuir* 2022; **38**, 15156-15164.

[48] T Wang, X Chen, C Ju and C Wang. Calcium signaling in plant mineral nutrition: From uptake to transport. *Plant Communications* 2023; **4**, 100678.

[49] J Batchelor-McAuley, A Martinez-Marrades, PA Glaeser, DP Sigman and RG Compton. Calcium carbonate dissolution from the laboratory to the ocean: Kinetics and mechanism. *Chemistry - A European Journal* 2022; **28**, e202202290.

[50] MM Nazir, M Noman, T Ahmed, S Ali, Z Ulhassan, F Zeng and G Zhang. Exogenous calcium oxide nanoparticles alleviate cadmium toxicity by reducing Cd uptake and enhancing antioxidative capacity in barley seedlings. *Journal of Hazardous Materials* 2022; **438**, 129498.

[51] P Sharma and RS Dubey. Lead toxicity in plants. *Brazilian Journal of Plant Physiology* 2005; **17(1)**, 35-52.

[52] SK Panda and S Choudhury. Chromium stress in plants. *Brazilian Journal of Plant Physiology* 2005; **17(1)**, 95-102.

[53] International Molybdenum Association. *Molybdenum: An essential micronutrient*. International Molybdenum Association, London, 2013.

[54] UC Gupta. *Molybdenum in agriculture*. Cambridge University Press, Cambridge, England, 1997.